Delft University of Technology

Automated planning of curved needle channels in 3D printed patient-tailored applicators for cervical cancer brachytherapy

Straathof, Robin; van Vliet-Pérez, Sharline M.; Kolkman-Deurloo, Inger Karine K.; Wauben, Linda S.G.L.; Nout, Remi A.; Heijmen, Ben J.M.; Rossi, Linda; Dankelman, Jenny; van de Berg, Nick J.

Important note
To cite this publication, please use the final published version (if applicable).
Please check the document version above.

IPEM
Institute of Physics and
Engineering in Medicine

PAPER • OPEN ACCESS

Automated planning of curved needle channels in 3D printed patient-tailored applicators for cervical cancer brachytherapy

View the article online for updates and enhancements.

Physics in Medicine & Biology

IPEM
Institute of Physics and
Engineering in Medicine

PAPER

Automated planning of curved needle channels in 3D printed patient-tailored applicators for cervical cancer brachytherapy

Robin Straathof[1,2,*] , Sharline M van Vliet-Pérez[1,2] , Inger-Karine K Kolkman-Deurloo[2] ,
Linda S G L Wauben[1] , Remi A Nout[2] , Ben J M Heijmen[2] , Linda Rossi[2] , Jenny Dankelman[1]
and Nick J van de Berg[1,3]

1 Department of BioMechanical Engineering, Delft University of Technology, Delft, The Netherlands
2 Department of Radiotherapy, Erasmus MC Cancer Institute, University Medical Centre Rotterdam, Rotterdam, The Netherlands
3 Department of Gynaecological Oncology, Erasmus MC Cancer Institute, University Medical Centre Rotterdam, Rotterdam, The Netherlands
* Author to whom any correspondence should be addressed.
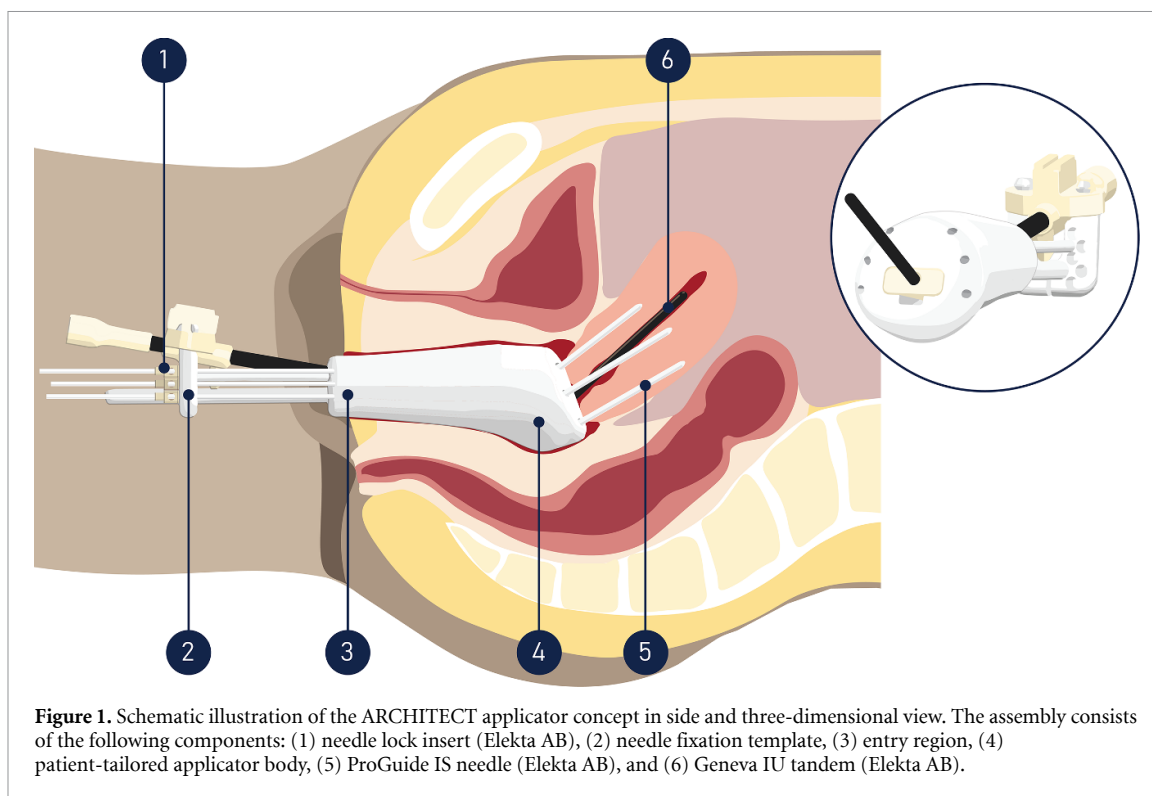
E-mail: r.straathof-1@tudelft.nl

Abstract

Purpose. Patient-tailored intracavitary/interstitial (IC/IS) brachytherapy (BT) applicators may increase dose conformity in cervical cancer patients. Current configuration planning methods in these custom applicators rely on manual specification or a small set of (straight) needles. This work introduces and validates a two-stage approach for establishing channel configurations in the 3D printed patient-tailored ARCHITECT applicator. *Methods.* For each patient, the patient-tailored applicator shape was based on the first BT application with a commercial applicator and integrated connectors to a commercial (Geneva) intrauterine tube and two lunar ring channels. First, a large candidate set was generated of channels that steer the needle to desired poses in the target region and are contained in the applicator. The channels' centrelines were represented by Bézier curves. Channels running between straight target segments and entry points were optimised and refined to ensure (dynamic) feasibility. Second, channel configurations were selected using geometric coverage optimisation. This workflow was applied to establish patient-tailored geometries for twenty-two patients previously treated using the Venezia applicator. Treatment plans were automatically generated using the in-house developed algorithm BiCycle. Plans for the clinically used configuration, TP_{clin}, and patient-tailored configuration, TP_{arch}, were compared. *Results.* Channel configurations could be generated in clinically feasible time (median: 2651 s, range 1826–3812 s). All TP_{arch} and TP_{clin} plans were acceptable, but planning aims were more frequently attained with patient-tailored configurations (115/132 versus 100/132 instances). Median CTV_{IR} D_{98} and bladder D_{2cm^3} doses significantly improved ($p < 0.001$ and $p < 0.01$ respectively) in TP_{arch} plans in comparison with TP_{clin} plans, and in approximately half of the patients dosimetric indices improved. *Conclusion.* Automated patient-tailored BT channel configuration planning for 3D printed applicators is clinically feasible. A treatment planning study showed that all plans met planning limits for the patient-tailored configurations, and in selected cases improved the plan quality in comparison with commercial applicator configurations.

1. Introduction

1.1. Clinical motivation

High-dose-rate (HDR) brachytherapy (BT) is an essential component in the curative treatment of locally advanced cervical cancer in combination with external beam radiotherapy (EBRT) and concomitant chemotherapy (Pötter *et al* 2007). Conventional BT applicators enable positioning of the radioactive source in: (1) intracavitary (IC) channels, such as the intrauterine (IU) tandem and ring or ovoid channels, and (2) interstitial (IS) needles inserted in tissue in or near the tumour. Despite high local control rates (Fokdal *et al*

Figure 1. Schematic illustration of the ARCHITECT applicator concept in side and three-dimensional view. The assembly consists of the following components: (1) needle lock insert (Elekta AB), (2) needle fixation template, (3) entry region, (4) patient-tailored applicator body, (5) ProGuide IS needle (Elekta AB), and (6) Geneva IU tandem (Elekta AB).

2016), some disadvantages are still associated with standard IC/IS applicators. First, standard applicators may be ill-adapted to large tumours or unfavourable anatomies (Fokdal *et al* 2016, Mahantshetty *et al* 2019, Serban *et al* 2020). These patients require insertion of parallel and oblique needles using advanced applicators through fixed guide holes (Lindegaard *et al* 2016, Petric *et al* 2016, Serban *et al* 2021). Transperineal needles may be added to improve dose conformity (Bailleux *et al* 2016), but this technique relies heavily on experience of the clinician. Second, a relatively high incidence of mild to moderate morbidity is still observed (Fortin *et al* 2016, Fokdal *et al* 2018), impacting quality of life (Kirchheiner *et al* 2016). Lastly, applicators must ensure a good fit and contact with the tissue, and facilitate reliable placement (Tanderup *et al* 2008), which may not be possible in patients with narrow or irregular vaginal vaults (Nilsson *et al* 2015).

Patient-tailored applicators that have been proposed previously may increase dose conformity (Wiebe *et al* 2015, Lindegaard *et al* 2016, Logar *et al* 2019, Zhang *et al* 2019, Serban *et al* 2021, Cobussen *et al* 2023), and ensure reliable placement (Magné *et al* 2010). For these applicators, the majority of methods to determine customised source channel configurations require manual specification, and only some partially automated methods have been proposed (Garg *et al* 2013, Duan *et al* 2014, Patil *et al* 2015, Zhang *et al* 2019). However, optimality and convergence of these methods rely on expertise of the clinician or the quality of a small set of a priori specified (straight) dwell segments. Within the ARCHITECT project, a single use patient-tailored applicator concept has been developed (figure 1), for which IC/IS channel configuration generation is automated. The ARCHITECT concept applicator design consists of two 3D printed halves that contain the optimised channels, and are proposed to connect to a commercially available IU tandem (Geneva, Elekta AB, Stockholm, Sweden). The workflow for this applicator is similar to that of commercial applicators, including applicator placement, needle insertion, and treatment planning. By basing placement of the needles on the patient's anatomy, this applicator is expected to improve dose conformity, and subsequently outcome. This paper describes the development and validation of software for automated needle channel planning in these patient-tailored applicators.

1.2. Related work

HDR-BT treatment plan optimisation is a complex multi-objective problem in which target coverage and organ at risk (OAR) dose must be balanced, and goal values and limits (respectively soft and hard constraints) on dose-volume histogram (DVH) parameters must be respected (Pötter *et al* 2018). In case of cervical cancer, prevention of hot or cold spots, and relative contribution of applicator components also need to be taken into account (Oud *et al* 2020, Rossi *et al* 2024). The resulting multi-objective model is therefore not convex, linear, nor smooth. Although most work in HDR-BT optimisation has focussed on dwell time optimisation, several methods have been proposed for implant configuration optimisation

(Morén *et al* 2021). The majority of these algorithms have been developed for HDR-BT of the prostate assuming straight needle paths and small candidate needle sets. One class of methods aims to solve the integrated problem of dwell time optimisation and needle selection, which results in a mixed integer program that cannot be solved in clinically feasible time (Gorissen *et al* 2013). Therefore, heuristics are applied and DVH constraints relaxed to linear or quadratic dose-calculation point penalty functions at the expense of guaranteed optimality, convergence, and plan feasibility (Zhang *et al* 2019, Wang *et al* 2021). In addition, the selected number of needles may be predetermined or used in a separate optimisation layer (Karabis *et al* 2009, Holm *et al* 2016). Aforementioned models use a single (weighted sum) objective, but bi-objective optimisation has also been proposed (Sadowski *et al* 2017, van der Meer *et al* 2018). Another class of methods iteratively reduces or increases the number of needles based on their contribution to the planning objective or dwell times (Guthier *et al* 2016, 2017, Bélanger *et al* 2024). In the last class of methods, implant configuration optimisation is based on geometry and fully decoupled from dwell time optimisation. Model formulations in this class have been based on the set cover problem (Siauw *et al* 2012), and centroidal voronoi tessellation (Poulin *et al* 2013, Chatigny *et al* 2022). Despite this simplification, clinically acceptable configurations can be returned in short optimisation times that perform similar to other methods mentioned above (Guthier *et al* 2017).

Several articles have described motion planning methods for curved HDR-BT IC channel configurations. In these works, a set of (straight) dwell segments is a priori determined and needle or source behaviour is assumed to be nonholonomic. The approaches used curvature-constrained rapidly-exploring random trees (Garg *et al* 2013), sequential quadratic programming (Duan *et al* 2014), and a two-stage planning approach, with rapidly-exploring random trees and local (multi-) trajectory optimisation (Patil *et al* 2015). While the proposed methods are of interest, they have some limitations: (1) convergence cannot be guaranteed for a given dwell segment configuration, (2) the assumption of nonholonomic kinematics imposes a high-dimensional configuration space resulting in clinically infeasible optimisation times for multi-trajectory planning, and (3) quality of the motion planning solutions depends on the initialisation or channel planning order.

To address the above issues of convergence, optimality and running times, we introduce a two-stage approach in which first a large candidate set of feasible needle channel trajectories is generated, and second an array of optimal channel configurations is returned using geometric coverage optimisation. The channel centrelines are represented by Bézier curves. These provide a natural parameterisation of smooth and dynamically feasible trajectories in 3D space, and are therefore frequently used in real-time motion planning of vehicles such as quadrotors (Mellinger and Kumar 2011, Richter *et al* 2016, Gao *et al* 2018). In addition, for a common approximator of the minimal bending energy of an inextensible Bézier curve, a closed-form expression exists (Veltkamp and Wesselink 1995). Similar formulations have been used for modelling flexible instruments (Fauser *et al* 2019, Rajesh and Khatait 2021).

1.3. Contribution

The aim of this work is to introduce an automated approach for generating a large set of feasible needle channel trajectories, and for selecting sets of optimal configurations that can be integrated in patient-tailored applicators for locally advanced cervical cancer BT. Dosimetric advantages of these patient-tailored configurations are illustrated through virtual automated treatment planning in a representative patient cohort.

2. Materials and methods

2.1. General overview

The proposed method for generating and selecting optimal configurations for the ARCHITECT applicator is outlined in figure 2, and pseudocode of the software is depicted in algorithm 1. The workflow can easily be aligned with the current clinical workflow and requires additional user input only for the determination of the outer shape of the applicator, target region selection, final needle configuration selection and quality control. All code is implemented in MATLAB (R2021b, MathWorks, Natick, Massachusetts, USA). Automated multi-criteria dwell-time optimisation is performed with the in-house developed optimiser BiCycle (Oud *et al* 2020, Rossi *et al* 2024). For geometry processing, three toolboxes are used: gptoolbox (Jacobson 2023), GIBBON (Moerman 2018), and MeshFix (Attene 2010). Computations are performed in the computing cluster of the Erasmus MC, utilising two 8-core 2.90 GHz Intel Xeon E50-2690 CPUs. Several processes are run in parallel using 12 computing threads.

Figure 2. Schematic overview of the proposed method for generating the patient-tailored needle channel configuration. (1) Patient data are imported and a clinical reference plan is established. For trajectory and coverage planning, (2) structures are processed into meshes, and (3) applicator geometry and planning space are determined. To generate a candidate set of channels, iteratively (4a-c) an IS and entry segment are sampled and a feasible curvature-minimising channel is computed. For the selection of a configuration of channels from the candidate set, (5a-5b) geometric coverage optimisation is performed generating a series of feasible configurations. From the resulting solution space a patient-tailored configuration is selected, and (6) treatment planning is performed.

2.2. Process overview

2.2.1. Importing patient data and clinical plan

In this step, data from the first BT application with commercial applicator and gauze packing are obtained. The patient-tailored applicator's body is based on this distended shape of the vaginal cavity. Therefore, in addition to the target volumes and OARs, contouring of the vaginal cavity is performed in MIM (MIM Software Inc., Cleveland, Ohio, USA), resulting in segmentation list $\mathcal{S}$ (RTStruct file). MR images $\mathcal{I}$ and treatment plan $\mathcal{P}$ (RTPlan file) are obtained from Oncentra Brachy (version 4.6, Elekta AB), of which the

Algorithm 1. Pseudocode used in this work for the generation of the ARCHITECT applicator geometry containing optimised needle channels and corresponding treatment plan.

Algorithm 1 : $(\mathcal{A}, \mathrm{TP_{arch}}) \leftarrow \mathrm{ChannelPlanner}(\mathcal{D}, \mathcal{T}, Q_0, id, n_{IS}, n_{sol}, t, w, \Delta, \varepsilon_{max}, \kappa_{max}, \lambda)$

1. **Importing patient data and clinical plan**
1 : $(\mathcal{I}, \mathcal{P}, \mathcal{S}) \leftarrow \mathrm{ImportPatient}(id)$ #*Get data*
2 : $\mathrm{TP_{clin}} \leftarrow \mathrm{BiCycle}(\mathcal{P}, \mathcal{S})$ #*Plan clinical config.*
2. **Processing anatomical structures**
3 : $\mathcal{S}_{tri} \leftarrow \mathrm{InterpStructure}(\mathcal{S})$ #*Get triangle mesh*
3. **Determining applicator geometry and coverable region**
4 : $\mathcal{A} \leftarrow \mathrm{ImportApplicator}(\mathcal{P})$ #*Get geometry*
5 : $(\mathcal{A}, \mathcal{C}_{free}, \mathcal{E}_h) \leftarrow \mathrm{ProcessApp}(\mathcal{A}, \mathcal{E}, \mathcal{S}_{tri}, t, w, \lambda)$ #*Process geometry and free space*
6 : $(\mathcal{C}_{exit}, \mathcal{T}) \leftarrow \mathrm{CoverRegion}(\mathcal{A}, \mathcal{T})$ #*Get cover regions*
4. **Determining channel candidate set**
7 : $\mathcal{N}_{IS} \leftarrow \mathrm{GenerateChannel}(\mathcal{A}, \mathcal{C}_{free}, \mathcal{C}_{exit}, \mathcal{E}_h, Q_0, \mathcal{T}, n_{IS}, \kappa_{max})$ #*Algorithm 2*
5. **Selecting needle channels using integer programming**
8 : $(I, \boldsymbol{\varepsilon}) \leftarrow \mathrm{Cover}(\mathcal{N}_{IS}, \mathcal{S}_{tri}, \mathcal{T}, \Delta, \varepsilon_{max})$ #*Get coverage*
9 : $V \leftarrow \mathrm{Collision}(\mathcal{N}_{IS}, t, w)$ #*Get collision*
10 : $\mathcal{Z}_s \leftarrow \mathrm{SelectChannel}(\mathcal{E}_h, \mathcal{N}_{IS}, V, I, n_{sol}, \boldsymbol{\varepsilon}, \varepsilon_{max})$ #*Algorithm 3*
6. **Generating plan for patient − tailored configuration**
11 : $\mathcal{P}' \leftarrow \mathrm{ModifyPlan}(\mathcal{P}, \mathcal{Z}_s)$ #*Get new plan file*
12 : $\mathrm{TP_{arch}} \leftarrow \mathrm{BiCycle}(\mathcal{P}', \mathcal{S})$ #*Plan ARCH. config.*
13 : **return** $(\mathcal{A}, \mathrm{TP_{arch}})$ #*Export files*

---

latter defines the clinically used configuration. Automated multi-criterial treatment planning is performed with BiCycle to establish a clinical reference plan, $\mathrm{TP_{clin}}$.

2.2.2. Processing anatomical structures

In order to enable efficient computations, the code works with triangular meshes to represent structures and the outer applicator geometry. Triangular meshes, $\mathcal{S}_{tri}$, of regions of interest are obtained from contours based on an interpolation method capable of handling branching, similar to that proposed by Sunderland *et al* (2015). In our approach, however, overlap of contours is checked by exact methods in order to deal with concave contours. Meshes are subsequently closed, processed, and subjected to a series of quality control checks.

2.2.3. Determining applicator geometry and coverable region

The concept ARCHITECT applicator embodiment attaches to the Geneva IU tandem and contains two lunar-shaped ring channels similar to the Venezia applicator (Elekta AB). Geometries of these components are matched and aligned with the clinically used configuration, and added to applicator structure $\mathcal{A}$. The outer geometry of the ARCHITECT applicator is further based on contouring of the vaginal cavity and (user) specification of an entry region $\mathcal{E}$. A swept tapered section connects the patient-tailored top to a circular entry region with a diameter of 25 mm. Laplacian smoothing in accordance with a user parameter λ is performed. The applicator body is split in two halves (the distinction between halves is henceforth omitted), and connectors to the IU tandem are created.

For the generation of the large candidate set of needle channels several inputs are required. A standard entry configuration is determined that enables four needles to be inserted per half, $\mathcal{E}_h$, next to the lunar ring IC channel. The available space in which the curved channels can be planned, called free space or $\mathcal{C}_{free}$, is computed by offsetting the outer geometry and IC channels by a distance equating to the channel lumen radius $w/2$ ($w = 2.8$ mm, enabling insertion of 6F needles) plus wall thickness t ($t = 1.0$ mm, ensuring wall integrity after 3D printing). The user is asked to specify a target structure $\mathcal{T}$, either the $\mathrm{CTV_{HR}}$ or the combined $\mathrm{CTV_{HR}}$ and $\mathrm{CTV_{IR}}$, which is to be geometrically covered. This structure is subdivided into coverable regions, each associated with an entry pose, to be used for biased IS segment sampling. In addition, an exit region $\mathcal{C}_{exit}$ is defined where IS needles exit the applicator.

2.2.4. Determining channel candidate set
2.2.4.1. Determining channel candidate set: Sampling IS dwell segments
A large candidate set is created by computing a set of n_{IS} ($n_{IS} = 200$ in this work) needle channels for each entry point, $\boldsymbol{e}_i \in \mathcal{E}_h$ in parallel (algorithm 2). A straight IS dwell segment is first generated by sampling exit region point $\boldsymbol{p}_C \in \mathcal{C}_{exit}$ and coverable region point $\boldsymbol{p}_T$, see figure 2 step 4a. Three sampling strategies are implemented for $\boldsymbol{p}_T$: uniform sampling on the surface of target structure $\mathcal{T}$, biased sampling according to the entry point, or biased sampling just outside the target surface. Segment feasibility is checked by determining

Algorithm 2. Pseudocode used in this work for fast needle channel generation.

Algorithm 2 : $\mathcal{N}_{IS} \leftarrow$ GenerateChannel$(\mathcal{A}, \mathcal{C}_{free}, \mathcal{C}_{exit}, \mathcal{E}_h, Q_0, \mathcal{T}, n_{IS}, \kappa_{max})$

1 : **parfor** $e_i \in \mathcal{E}_h$ **do**	
2 : **while** $n < n_{IS}$ **do**	
3 : $(\boldsymbol{p}_C, \boldsymbol{p}_T) \leftarrow$ SampleLine$(\mathcal{C}_{exit}, \mathcal{T})$	*#Sample IS segment*
4 : **if** is Feasible$(\mathcal{A}, \boldsymbol{p}_C, \boldsymbol{p}_T)$ **then**	*#Check feasibility*
5 : $(A_{eq}, \boldsymbol{b}_{eq}) \leftarrow$ Pose$(e_i, \boldsymbol{p}_C, \boldsymbol{p}_T)$	*#Constrain pose*
6 : $\mathbf{x} \leftarrow$ MinProg$(Q_0, A_{eq}, \boldsymbol{b}_{eq}, [], [])$	*#Plan Bézier curve*
7 : **if** CompCurv$(\mathbf{x}) \leq \kappa_{max}$ **then**	*#Check curvature*
8 : **if** $\neg$ Feasible$(\mathbf{x}, \mathcal{C}_{free}, \kappa_{max})$ **then**	*#Check feasibility*
9 : **repeat**	
10 : $\left[lb_\mu^l, ub_\mu^l \right] \leftarrow$ Bounds$(\mathbf{x}_\mu, \mathcal{C}_{free})$	*#Get $\mathcal{C}_{free}$ bounds*
11 : $\mathbf{x}_\mu \leftarrow$ MinProg$\left(Q_0, A_{eq}, \boldsymbol{b}_{eq}, lb_\mu^l, ub_\mu^l\right)$	*#Re-optimise curve*
12 : **until** *converged or stop*	
13 : **end if**	
14 : $\mathcal{N}_n \leftarrow$ CreateNeedle$(\mathbf{x})$	*#Get needle structure*
15 : $\mathcal{N}_{IS} \leftarrow \mathcal{N}_{IS} \cup \mathcal{N}_n$	*#Append to structure*
16 : $n = n + 1$	
17 : **end if**	
18 : **end if**	
19 : **end while**	
20 : **end parfor**	
21 : **return** $\mathcal{N}_{IS}$	

the angle (maximum angle 35°) with respect to the IU tandem (Serban *et al* 2021), and possibility for OAR perforation (minimum radial and axial distances 4 and 10 mm respectively). In addition, limits to the exit angle or region can be imposed to minimise deviations from a straight path in tissue.

2.2.4.2. Determining channel candidate set: minimum energy curve
Between each feasible IS dwell segment and given entry point a smooth IC channel is generated by planning a minimum energy Bézier curve. A Bézier curve $\boldsymbol{B}(t)$ of degree n is defined by a set of control points $\boldsymbol{c}^l \in X$ and Bernstein polynomials b_n^l:

$$\boldsymbol{B}(t) = \sum_{l=0}^{n} \boldsymbol{c}^l b_n^l(t), \qquad 0 \leq t \leq 1 \tag{1}$$

$$b_n^l(t) = \binom{n}{l} t^l (1-t)^{n-l}, \qquad l = 0, 1, \ldots, n \tag{2}$$

In this work quintic Bézier curves ($n = 5$) are used to represent the channel's centreline. As twist of the channel is not constrained and of minor influence on HDR-BT needle behaviour in applicator channels (Straathof *et al* 2024), we reduce the planning space to $\mathbb{R}^3$ and consider only bending energy E_{bend}, which can be approximated as follows (Veltkamp and Wesselink 1995, Gao *et al* 2018):

$$E_{bend}(\boldsymbol{B}) \approx \int_0^1 ||\boldsymbol{B}''(t)||^2 dt = \sum_{\mu \in \{x,y,z\}} \left(\frac{d^2 B_\mu(t)}{dt^2} \right)^2 dt = \mathbf{x}^T Q_0 x \tag{3}$$

Here, $\mathbf{x} = \text{vec}(X)$, and Q_0 is the Hessian matrix of which the construction is shown in the appendix. Specifying desired entry and exit poses of the needle channel as linear equality constraints (defined by A_{eq} and $\boldsymbol{b}_{eq}$), the minimisation procedure can be formulated as a quadratic programming (QP) problem, which can be solved fast using MATLAB's quadprog:

$$\min_{\mathbf{x}} \quad \mathbf{x}^T Q_0 \mathbf{x}$$
$$\text{s.t.} \quad A_{eq} \mathbf{x} = \mathbf{b}_{eq} \tag{4}$$

Curvature of the resulting trajectory is computed and the solution is discarded if the local maximum curvature exceeds a curvature constraint ($\kappa_{max} = 1/50$ mm^{-1}) (Laan *et al* 2019, Straathof *et al* 2024).

2.2.4.3. Determining channel candidate set: refine boundaries

IC channels need to be confined to the free space $\mathcal{C}_{\text{free}}$. As $\mathcal{C}_{\text{free}}$ has a relatively high convexity rank, initial feasibility checks are simplified by utilising the convex hull property of a Bézier curve and checking whether the control points lie in $\mathcal{C}_{\text{free}}$. If control points are not contained in $\mathcal{C}_{\text{free}}$, feasibility is checked for a fine discretisation of the curve. When the found trajectory is still infeasible, it is re-optimised taking into account applicator boundary constraints. In order to retain the fast quadratic programming formulation and making use of the trajectory decomposition in $\mathbb{R}^3$, the complex nonconvex boundary constraints are converted into lower and upper bounds on individual control points per direction μ, $\left[\text{lb}_\mu^l, \text{ub}_\mu^l \right]$, as has been described previously (Zhao *et al* 2019). The problem is re-optimised alternating the direction of the projections until all control points or the curve are in $\mathcal{C}_{\text{free}}$, or until a maximum number of iterations is exceeded, see the loop at steps 4b and 4c in figure 2. Once a feasible solution has been found, the channel $\mathcal{N}_n$ is generated with dwell positions 5 mm apart and is appended to the set $\mathcal{N}_{\text{IS}}$.

2.2.5. Selecting needle channels using integer programming

From the large candidate set, a small set of needle channels must be selected that is feasible, and enables treatment plans to meet clinical objectives, referred to as the patient-tailored configuration. The channel selection algorithm is based on geometric coverage and inspired by NPIP (Siauw *et al* 2012), which attempts to solve a set cover problem with conflicts. To ensure convergence and consider target region coverage as the main priority, the channel selection problem is formulated as a max k-cover problem (MKCP) with conflicting pairs instead. In our formulation of max k-cover, the inputs are a collection of sets $\mathcal{U} = \{\mathcal{U}_1, \mathcal{U}_2, \ldots, \mathcal{U}_{|\mathcal{N}_{\text{IS}}|}\}$ that signify which dose points $t_m \in \mathcal{T}$ are covered by a needle. The integer k specifies how many sets may be chosen, and the goal is to maximise the cardinality of the union of selected sets, i.e. $|\mathcal{U}'|$, where $\mathcal{U}' \subseteq \mathcal{U}$. In addition, channels or needles that are in collision may not be selected simultaneously, as distinguished by the pairwise validity matrix V. An integer linear program formulation of this problem is the following:

$$
\begin{aligned}
\max \quad & \sum_{t_m \in \mathcal{T}} z_m && \text{(MKCP)} \\
\text{s.t.} \quad & \sum x_s \leq k \\
& \sum_{s : t_m \in U_s} x_s \geq z_m \\
& x_y + x_z \leq 1 && \forall (y, z) \in V \\
& x_s \in \{0, 1\} \\
& z_m \in \{0, 1\} && (5)
\end{aligned}
$$

Here, z_m is an integer which marks whether the mth dose point is covered, and x_s an integer which indicates whether the sth needle channel is selected to be part of $\mathcal{U}'$. Pairwise collision constraints are defined by $x_y + x_z \leq 1$, $\forall (y, z) \in V$. The formulation in equation (5) can be cast in the compact form $\min \left\{ f^T \hat{z} \,\middle|\, A_{\text{ineq}} \hat{z} \leq b_{\text{ineq}} \wedge \hat{z} \in \{0, 1\}^{|\mathcal{N}_{\text{IS}}| + |t_m \in \mathcal{T}|} \right\}$, where $\hat{z} = [x; z]$. Pseudocode for this procedure is outlined in algorithm 3.

2.2.5.1. Computing coverage and collision matrices

A channel $\mathcal{N}_s$ is defined to 'cover' dose point t_m if it contains a dwell position d_p such that the Euclidean distance to the dose point is less than the coverage radius ε (Siauw *et al* 2012). Whereas in previous formulations the coverage radius is fixed, i.e. assuming a constant dwell time for every position, we scale the coverage radius depending on the proximity of the dwell position to any of the OARs:

$$
\varepsilon_p = \min \left(\sqrt{\tfrac{\Delta_o}{\Delta_\mathcal{T}}} \| d_p - t_o \|_2 , \varepsilon_{\max} \right) \qquad (6)
$$

Here, subscript o is used to denote any of the OARs, and a planning aim ratio $\Delta_o / \Delta_\mathcal{T}$ (e.g. $D_{2\text{cm}^3}$ versus D_{90}) is used to scale the coverage radius. The maximum coverage radius $\varepsilon_{\max}$ is defined as a fraction (here empirically determined at 0.4) of the radius of the minimum enclosing sphere around the target structure. Dose points are generated in $\mathcal{T}$ using a regular grid with 3.0 mm spacing. This enabled fast (parallel) distance check queries between grid points and dwell segments, adaptively using line–line, point–line, and point–point checks. The resulting coverage matrix is denoted by I.

In order to prevent collisions of the channels or needles, minimum inter-centreline distances must be respected determined by lumen diameter w and channel wall thickness t. Channel and dwell segment

Algorithm 3. Pseudocode used in this work for needle channel selection.

Algorithm 3 : $\mathcal{Z}_s \leftarrow$ SelectChannel $(\mathcal{E}_h, \mathcal{N}_{IS}, V, I, n_{sol}, \boldsymbol{\varepsilon}, \varepsilon_{max})$

---

1 : **parfor** $k \in [1, |\mathcal{E}_h|]$ **do**
2 :   **while** $n < n_{sol}$ **do**
3 : $(A_{ineq}, \boldsymbol{b}_{ineq}) \leftarrow$ CovConst (V, I, k) #*Get matrix form*
4 : $\widehat{\boldsymbol{z}}_{n,k} \leftarrow$ IntProg $(\boldsymbol{f}, A_{ineq}, \boldsymbol{b}_{ineq})$ #*Solve program*
5 : $(f_{\mathcal{T}}, f_o) \leftarrow$ Obj $(\widehat{\boldsymbol{z}}_{n,k}, \boldsymbol{f}, \boldsymbol{\varepsilon}, \varepsilon_{max})$ #*Get function value*
6 : $F \leftarrow$ AddPareto $(f_{\mathcal{T}}, f_o)$ #*Add to Pareto plot*
7 : $V \leftarrow V \cup$ Const $(\widehat{\boldsymbol{z}}_{n,k})$ #*Mark as colliding*
8 : $\mathcal{Z} \leftarrow \mathcal{Z} \cup$ AddNeedle $(\mathcal{N}_{IS}, \widehat{\boldsymbol{z}}_{n,k})$ #*Append to structure*
9 : $n = n + 1$
10 : **end while**
11 : **end parfor**
12 : $\mathcal{Z}_s \leftarrow$ SelectConfig $(F, \mathcal{Z})$ #*User select configuration*
13 : **return** $\mathcal{Z}_s$

---

collision checks are sped up by first considering the entry point of the potentially colliding pair. If required, straight IS dwell segment distance checks or discretised IC channel collision checks are performed, the latter by approximating curved channel centrelines with a sequence of straight segments. The resulting collision matrix is denoted by V. To reduce the number of collision constraints, pairwise collision constraints are turned into group cuts by considering all collision pairs for a certain channel (Kulkarni-Thaker *et al* 2021).

2.2.5.2. Performing integer needle optimisation
The integer linear program in equation (5) is solved for a range of values of k, that is, the number of selected needle channels. For each k, the intlinprog solver with default settings in MATLAB is called to find a solution. This solver uses among others relaxation, heuristics and branch-and-bound. Once a feasible non-empty solution $\widehat{\boldsymbol{z}}$ is found, the configuration is added to the matrix of conflicts V and the problem is re-solved to diversify the found solutions for a given number of channels. For a configuration, we define a coverage score $f_{\mathcal{T}} = (\sum_{\boldsymbol{t}_m \in \mathcal{T}} z_m) / |\boldsymbol{t}_m \in \mathcal{T}|$ expressing how many points are covered (0 = none covered, 1 = all dose points covered), and an OAR score $f_o = \text{std}\left(\left\{\left(\varepsilon_{max} - \varepsilon_p\right)/\varepsilon_{max} | \boldsymbol{d}_p \in \mathcal{N}_s : \boldsymbol{x}_s = 1 \text{ for some } s\right\}\right)$ quantifying the proximity of dwell positions to OARs (0 = no overlap with OARs, 1 = full overlap with OARs). The tuple $\{f_{\mathcal{T}}, f_o\}$ can be plotted for all found sets to generate a Pareto front F and other near-optimal solutions (Sadowski *et al* 2017, Bélanger *et al* 2020). One can explore this solution space trading off the coverage score, OAR score, or the number of IS needles (see schematic overview in step 5b, figure 2). A graphical user interface is provided to show the selected patient-tailored configuration. For this study, a configuration with the same number of IS needles as the clinical configuration was automatically selected based on a combined coverage and OAR score.

2.2.6. Generating plan for patient-tailored configuration
Dwell time optimisation with BiCycle is performed for the selected ARCHITECT configuration to obtain the plan TP_{arch}. Treatment plan parameters are computed, and the final applicator geometry $\mathcal{A}$ is created.

2.3. Patient evaluation
For this study, first fractions of twenty-two patients with FIGO stage IB3-IV locally advanced cervical cancer were considered that were treated with the IC/IS Venezia applicator (Elekta AB) between 2021 and 2022. There were no other patient selection criteria. Treatments included EBRT (25 fractions of 1.8 Gy) and MRI-guided BT (3-4 fractions). Patient details are shown in table 1. For both TP_{clin} and TP_{arch} plans, the clinical BT wish-list for cervical carcinoma was used with BiCycle automated treatment planning that adheres to the EMBRACE II aims and considers dose to the CTV_{HR}, CTV_{IR}, OARs (bladder, rectum, sigmoid and bowel) and dose points (Point A, vaginal top points, and recto-vaginal point) (Pötter *et al* 2018), as well as smoothing and relative needle contribution (Rossi *et al* 2024). Planning aims and limits for the full treatment were converted to those for a single fraction considering the amount of fractions the patient received in clinic. Clinical IS needle depth measured from applicator top was estimated based on the most distal DP in the clinical plan.

The ability of our approach to generate high-quality patient-tailored configurations was demonstrated by generating plans with the same number of needles as used in the clinical plan. Clinically relevant DVH-parameters in accordance with EMBRACE II aims, and the conformity index $\left(\text{COIN} = \frac{V_{100}^{\text{CTV}_{HR}}}{V^{\text{CTV}_{HR}}} \cdot \frac{V_{100}^{\text{CTV}_{HR}}}{V_{100}^{\text{Total}}} \cdot \prod \left(1 - \frac{V_{100}^o}{V^o}\right)\right.$ with superscript o denoting OARs) (Baltas *et al* 1998), were extracted

Table 1. Patient characteristics used in the virtual planning study ($n = 22$).

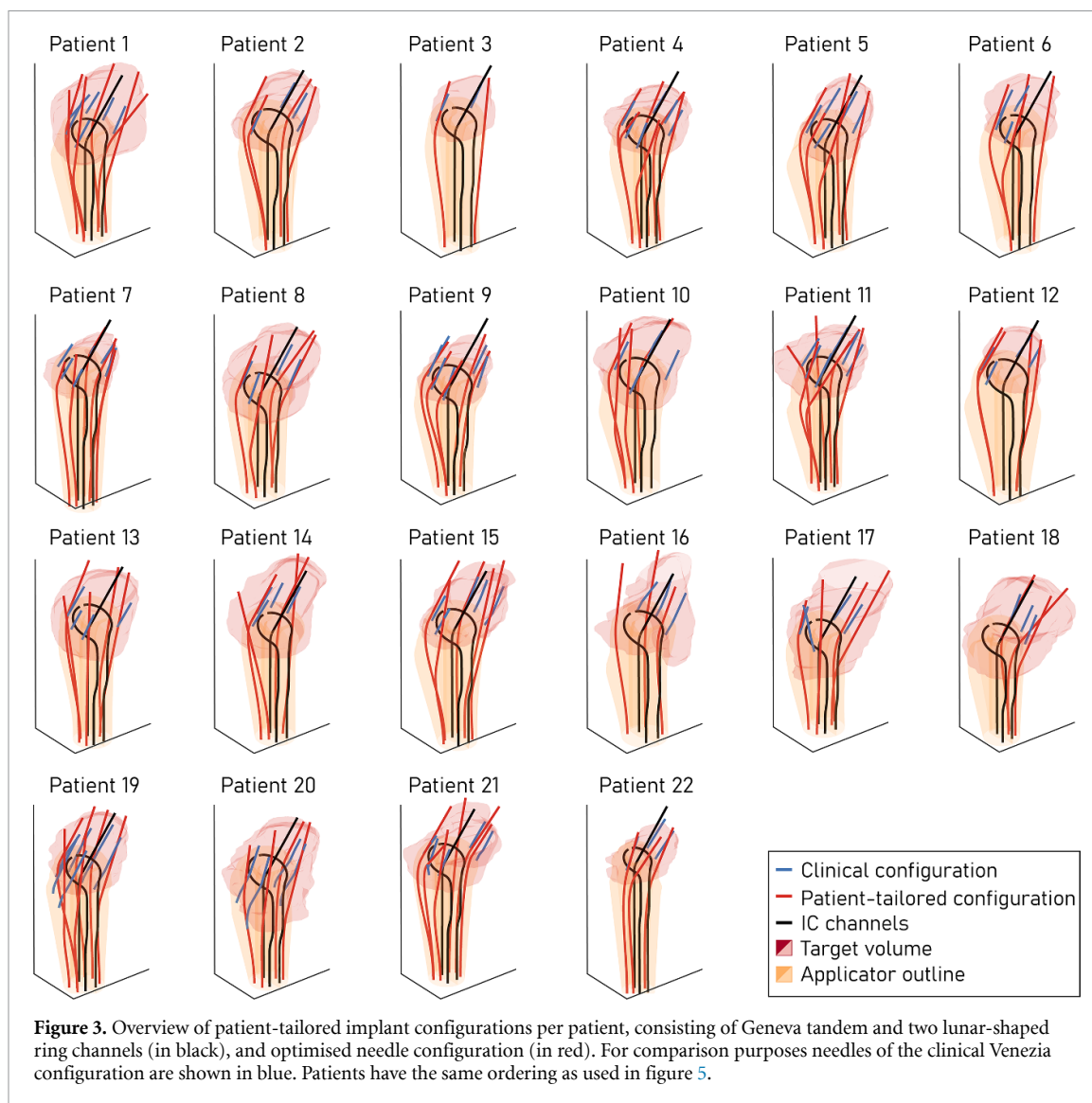| Parameter	Value
FIGO 2018 stage (*n*,%)	
IB	2 (9)
II	5 (23)
III	13 (59)
IVA	2 (9)
Number of BT fractions (*n*,%)	
3	17 (77)
4	5 (23)
Median (range) CTV_{HR} volume at BT (cm^3)	34.7 (13.3 − 52.1)
Median (range) number of needles	4 (2 − 6)

from TP_{clin} and TP_{arch} plans. Results for the GTV_{res} and bowel are not shown here, as the former was not considered in the wish-list, and for the latter planning aims were always highly met. To allow for comparisons between patients treated with a different number of fractions, the projected total treatment dosimetric parameters were computed assuming remaining doses would be constant throughout the remaining number of fractions. Statistical significance between the medians of two (paired) groups was determined using paired Wilcoxon signed-rank or Wilcoxon rank-sum tests, with Bonferroni-Holm correction applied and significance level $\alpha = 0.05$. Correlations were investigated using Spearman's rank correlation.

3. Results

For all patients, a patient-tailored applicator configuration could be generated. Clinically used and selected patient-tailored channel configurations are shown in figure 3 for all 22 patients. Patient-tailored needles were often not parallel to the IU tandem and instead diverged in the direction of target volume extension. Coverage scores (median, IQR) were significantly higher for the patient-tailored configuration in comparison with the clinical configuration (0.88; 0.85–0.91 versus 0.83; 0.74–0.88, $p < 0.01$, $z = 3.88$), but proximity to OARs also increased significantly (0.14; 0.12–0.17 versus 0.08; 0.06–0.11, $p < 0.01$, $z = 3.07$). To prevent collisions with the IC lunar ring channels and allow for sufficient wall thickness for 3D printing, needles exited the applicator more laterally than the clinically implanted needles. Insertion depth (median; IQR) measured from applicator top was significantly greater ($p < 0.001$, $z = 10.21$) for the patient-tailored needles (37 mm; 32–44 mm) than the estimated depth of the clinically implanted needles (24 mm; 22–28 mm). Median computation times for patient-tailored needle channel generation (algorithm 3) and the full applicator development (algorithm 1) were respectively 407 s (range 56–498 s) and 2651 s (range 1826–3812 s).

All generated TP_{clin} and TP_{arch} plans were considered to be acceptable considering that no EMBRACE II limits were exceeded (figure 4). However, with the clinical configurations, goal values for the CTV_{HR} D_{90}, CTV_{HR} D_{98}, or CTV_{IR} D_{98} were not met in 4 (18%), 2 (9%), or 5 (23%) patient cases respectively, opposed to 0 (0%), 1 (5%), or 1 (5%) cases for the patient-tailored configurations. Similarly, OAR bladder, rectum and sigmoid D_{2cm^3} goal values were exceeded in 12 (55%), 4 (18%), and 5 (23%) of the clinical configurations, compared to 10 (45%), 2 (9%), and 3 (14%) for the patient-tailored configurations. For TP_{arch}/TP_{clin} plans the projected total treatment doses (median; IQR) were comparable for the CTV_{HR} D_{90} (90.1; 90.1–90.1 / 90.1; 90.0–90.1 Gy EQD2$_{\alpha/\beta = 10\,Gy}$), CTV_{HR} D_{98} (80.7; 77.6–81.3 / 79.0; 76.3–80.5 Gy EQD2$_{\alpha/\beta = 10\,Gy}$), rectum D_{2cm^3} (62.1; 52.2–64.6 / 60.4; 51.9–65.0 Gy EQD2$_{\alpha/\beta = 3\,Gy}$), and sigmoid D_{2cm^3} (63.8; 57.7–69.7 / 64.2; 57.9-69.8 Gy EQD2$_{\alpha/\beta = 3\,Gy}$). Median (IQR) projected total treatment CTV_{IR} D_{98} doses were significantly lower ($p < 0.001$, $z = -3.33$) for clinically used configurations in comparison to patient-tailored configurations, amounting to 60.2 (60.0–61.0) versus 60.5 (60.1–61.2) Gy EQD2$_{\alpha/\beta = 10\,Gy}$. Moreover, total treatment bladder D_{2cm^3} doses were favourable ($p < 0.01$, $z = 2.61$) for patient-tailored configurations at 79.9 (74.4–81.0) versus 80.6 (74.9–86.8) Gy EQD2$_{\alpha/\beta = 3\,Gy}$ for the clinical configurations. Median COIN scores were comparable for TP_{arch}/TP_{clin} (0.52; 0.48–0.57 / 0.53; 0.45–0.59). No significant difference in relative contribution of needles in TP_{arch} and TP_{clin} was found (23.2; 21.0–34.4 / 24.4; 19.4–39.5 %). Also, no correlations were observed between any of the tested variables, including number of needles, CTV_{HR} volume, coverage or OAR scores, and plan quality (DVH parameters).

Figure 5 shows the difference between fraction doses for TP_{arch} and TP_{clin} per patient and per dosimetric index. In several patients a better trade-off could be achieved with the patient-tailored configuration. As an example consider patient 15, in which the CTV_{HR} D_{90} for the clinical configuration was higher than the planning aim. For the patient-tailored configuration this index was reduced whilst still respecting the
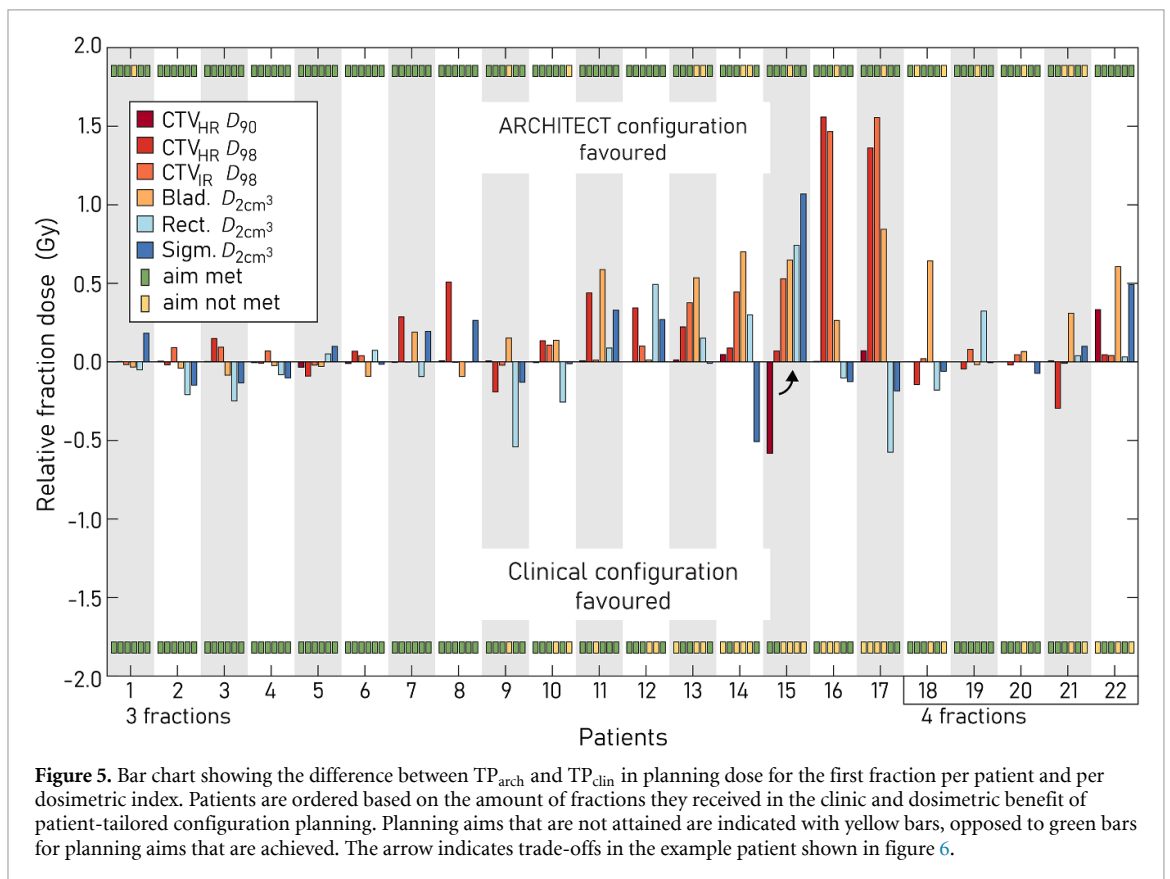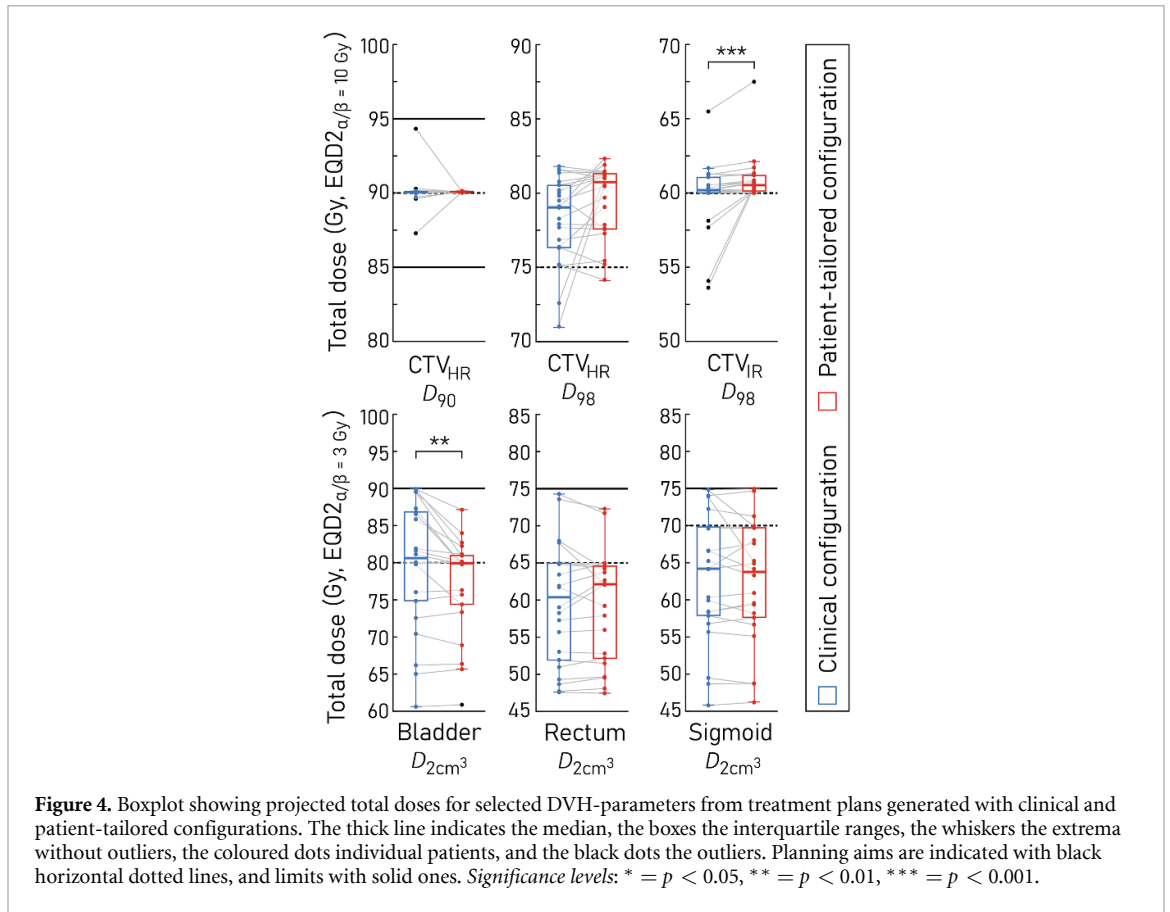
Figure 3. Overview of patient-tailored implant configurations per patient, consisting of Geneva tandem and two lunar-shaped ring channels (in black), and optimised needle configuration (in red). For comparison purposes needles of the clinical Venezia configuration are shown in blue. Patients have the same ordering as used in figure 5.

planning aim (marked by the black arrow), and the CTV_{IR} D_{98}, and bladder, rectum and sigmoid D_{2cm^3} improved. Representative axial and sagittal slices for the clinical and patient-tailored configuration for this patient are shown in figure 6. The positioning of needles in the patient-tailored configuration aligns better with the target region's geometry, resulting in lower OAR doses and improved target coverage.
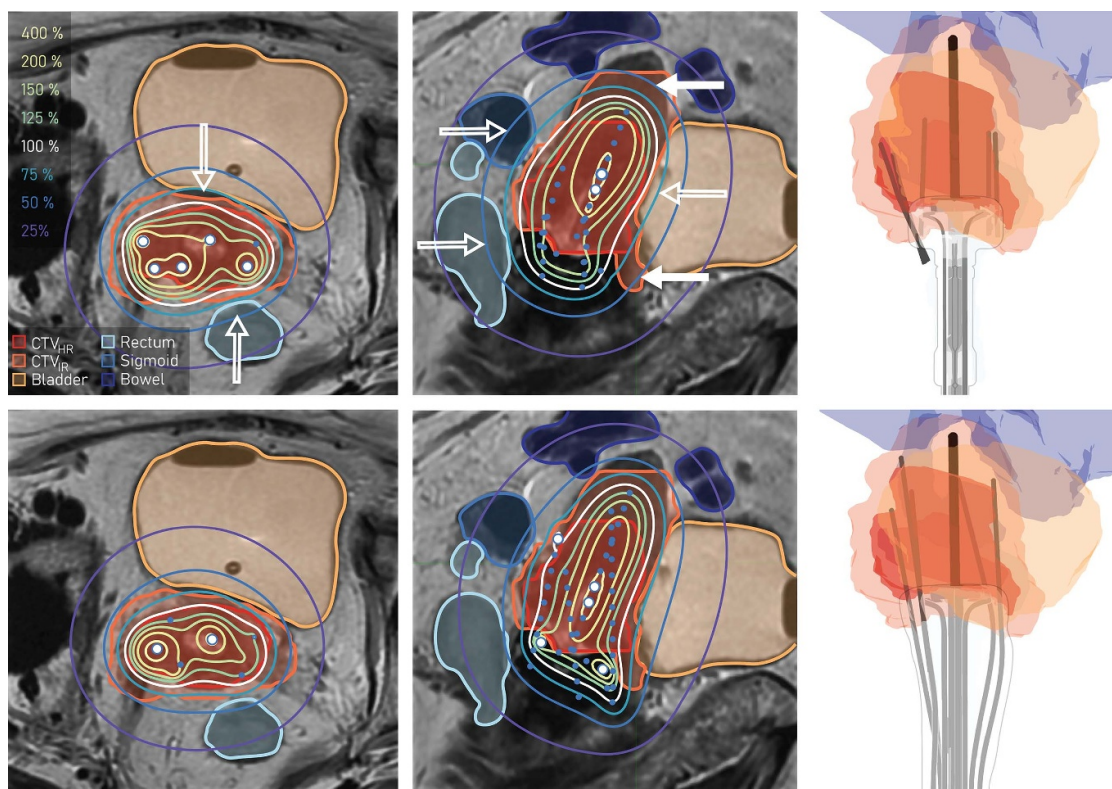
4. Discussion

This study introduces and dosimetrically validates an automated approach to generate and select channel configurations that can be integrated in patient-tailored applicators. In our proposed method, the patient-tailored applicator shape is derived from the distended vaginal geometry with a conventional BT applicator and packing in situ. Curved needle channels, of which the centreline is represented by a Bézier curve, are optimised and refined using quadratic programming between iteratively sampled straight IS segments and entry points. An array of sparse needle configurations is generated that maximises geometric coverage, from which the user can select a configuration and plan that best meets clinical objectives. In a treatment planning study for a patient cohort of 22 patients clinically acceptable treatment plans could be generated for clinical and patient-tailored configurations using the same number of IS needles. It was demonstrated that the dose conformity for the patient-tailored configurations was at least as good as for the clinical configurations in all patients, and that in a considerable amount of cases both the number of attained planning aims and dose conformity could be improved.

At the core of the automated approach to generate needle channels introduced in this work is fast quadratic programming. In order to ensure feasibility, nonconvex problem bounds are refined into bounds on the channel's control points. Whereas this method is computationally efficient, it requires: (1) a high

Figure 4. Boxplot showing projected total doses for selected DVH-parameters from treatment plans generated with clinical and patient-tailored configurations. The thick line indicates the median, the boxes the interquartile ranges, the whiskers the extrema without outliers, the coloured dots individual patients, and the black dots the outliers. Planning aims are indicated with black horizontal dotted lines, and limits with solid ones. *Significance levels*: * = $p < 0.05$, ** = $p < 0.01$, *** = $p < 0.001$.

Figure 5. Bar chart showing the difference between TP_{arch} and TP_{clin} in planning dose for the first fraction per patient and per dosimetric index. Patients are ordered based on the amount of fractions they received in the clinic and dosimetric benefit of patient-tailored configuration planning. Planning aims that are not attained are indicated with yellow bars, opposed to green bars for planning aims that are achieved. The arrow indicates trade-offs in the example patient shown in figure 6.

Figure 6. Dose distributions generated for the clinical configuration (upper row) and patient-tailored configuration (bottom row) for an example patient with FIGO 2018 IIIC1 cervical cancer (patient 15 in figure 5). Large blue dots with white filling indicate active dwell positions that are projected on the slice, and small blue dots indicate inactive dwell positions. The white line denotes the 100% isodose line prescribed to the CTV_{HR} D_{90}. Solid arrows mark regions in which the target region may be underexposed, whereas hollow arrows indicate OAR overexposure. With the patient-tailored configuration the dose distribution conforms better to the patient's geometry, improving coverage in superior and vaginal extensions. In addition, decreased dead space in the tip of the Geneva tandem (Elekta AB) in comparison with that of the Venezia (Elekta AB) allows for the dose distribution to extend in superior direction.

convexity rank of the bounded volume, (2) the existence of smooth feasible curves connecting start and entry poses, and (3) fast distance computations. If the first or second condition is not guaranteed, the volume may be decomposed in simple (convex) regions and (piecewise) trajectories may be confined to these regions (Mellinger and Kumar 2011, Gao *et al* 2018). Bézier curve replanning to enforce problem bounds can also be done via subdivision or degree elevation of the curve (Mehdi *et al* 2015). Inter-centreline distances were computed using straight line approximations, but could alternatively make use of culling approaches (Chang *et al* 2011).

Algorithms that integrate dwell time and implant configuration optimisation typically allow for tens of possible candidate needles in order to solve in clinically feasible times (Gorissen *et al* 2013, van der Meer *et al* 2018). Previously proposed methods to customise implant configurations for treatment of cervical cancer have therefore relied on expertise of the treating physician or quality of a small set of a priori specified (straight) needles or dwell segments. Instead, by decoupling dwell time and implant configuration planning and opting for geometric coverage optimisation for the latter, a large candidate set of potential needle trajectories can be used (Siauw *et al* 2012). Although treatment planning may be complex in gynaecological cancers due to the irregular anatomy, considering spatial coverage seems to be a reasonable simplification (Guthier *et al* 2017). The adaptive coverage radius defined in this work is based on the distance of a dwell position to OARs and scaled accordingly. Interestingly, coverage and OAR scores as defined in this study were not directly related to any of the evaluated dosimetric indices. Data-driven approaches using distance metrics are able to predict dosimetric indices accurately (Yusufaly *et al* 2020, Reijtenbagh *et al* 2022), and such approaches might be interesting to establish optimal configurations (Amit *et al* 2015).

For every patient in the cohort, a large set of channel trajectories could be generated in a limited amount of time (less than 500 s), and the end-to-end runtime for the full patient-tailored applicator generation was generally within one hour. User actions are limited to quality checks and selection of a final configuration, implying this can be integrated without disrupting the current clinical workflow. Computations can be sped up by providing heuristics in the needle selection program (Lee *et al* 2011), iterative constraint enforcement

(Lee *et al* 2014, Kulkarni-Thaker *et al* 2021), biasing of trajectory generation considering geometric spacing (reducing the candidate set size), and further parallelisation of subprograms.

Excellent dosimetric outcomes have been reported for patient-tailored applicator IC/IS configurations in earlier works (Lindegaard *et al* 2016, Serban *et al* 2021, Cobussen *et al* 2023), which were favourable in comparison with standard IC/IS applicators without oblique needles (Logar *et al* 2019, Zhang *et al* 2019). This study additionally indicates that patient-tailored applicators may outperform advanced standard applicators with oblique needles. The number of soft planning constraint violations was reduced for patient-tailored configurations in comparison with clinically used configurations. In addition, median CTV_{IR} D_{98} and bladder D_{2cm^3} dose improved significantly with the patient-tailored configuration. Similar effects were not observed for the rectum or sigmoid, likely due to the presence of the lunar ring channel which forced needles in the posterior direction. Needle channels can be planned to replicate the dwell positions in the ring-shaped channels of a conventional applicator, improving positioning flexibility and further increasing dose conformity (Lindegaard *et al* 2016, Serban *et al* 2021). Whereas these IC channels were automatically selected in the formulated integer program, our method can be extended to remove these channels if geometrically or dosimetrically favourable. It has been remarked that advanced IC/IS techniques also benefit smaller target volumes or less complex geometries (Fokdal *et al* 2013, Logar *et al* 2019, Serban *et al* 2020). In approximately half of the patients, dosimetric indices showed a clinically relevant improvement -and was not linked to target volume or complexity of the implant- which suggests that automated patient-tailored needle selection may help a patient population not typically associated with IC/IS application.

There are several limitations to the methodology introduced in this work. The primary focus of this study was to demonstrate the feasibility of our workflow and planning methods, and to validate the results in a small cohort. In the validation context of the ARCHITECT concept applicator, the applicator may be used only from the second application onwards as it is currently based on a first BT fraction with conventional applicator. In some institutes, a pre-BT MRI is performed with applicator (Fokdal *et al* 2013), which could also enable use of our patient-tailored applicator concept in the first fraction. Treatment plans for patient-tailored configurations to be used in the second application were compared in this exploratory study with those generated for the first clinical application. Several factors could have influenced this comparison. In the majority of patients in our cohort, the number of needles was increased in the second clinical application, with 1 (6/22 patients), 2 (4/22), 3 (2/22), or 4 (2/22) additional needles. In order to mitigate the effects of a suboptimal first implant, the number of needles was kept the same in the clinical and patient-tailored configurations. One of the benefits of our approach is that trade-offs between the number of needles and plan quality can be explored. In an upcoming planning study we will therefore investigate the potential benefits of informed needle selection. Additionally, more dwell positions were available for dwell time optimisation with patient-tailored configurations owing to a greater needle depth. Nevertheless, IS needle depths in the patient-tailored configurations were similar to those reported for other custom applicators (Serban *et al* 2021, Cobussen *et al* 2023). Although we routinely use pre-BT MRI without applicator and US to guide needle insertion in all BT applications, we tend to be cautious with regards to the number and depth of inserted needles in clinic to avoid OAR or blood vessel perforation. Insertion of patient-tailored needle configurations in practice might be challenged by similar factors such as the location of blood vessels or inability to visualise needles. A clinical study is needed to investigate whether preplanned configurations can be achieved. Moreover, the robustness of the patient-specific configurations to inter-application changes needs to be investigated. In particular, OAR positional and volumetric changes may alter the location of the D_{2cm^3} and make a pre-planned configuration suboptimal. The impact of such changes on plan quality may be limited (Logar *et al* 2019). In addition, robust treatment planning or implant configuration optimisation may be used to further reduce the potential effects of these changes (Jo *et al* 2021, Gerlach *et al* 2024). Lastly, several important planning parameters were not reported in this study, including the GTV_{res} D_{98}, point A, and rectovaginal point doses. These, along with overall plan quality, will be evaluated in an upcoming study.

5. Conclusions

This study presents a method for automatically generating and selecting brachytherapy needle channel configurations in patient-tailored applicators which was demonstrated to be clinically feasible. Treatment planning results illustrated that in approximately half of the patients, dosimetric indices showed a clinically relevant improvement for the patient-tailored configuration in comparison with the clinically used configuration using the same number of needles. The benefits of our two-stage approach are that it automatically generates a large set of candidates to select from, and that an array of sparse needle channel configurations is returned in all tested patient cases. Trade-offs in these solutions between plan quality and

the amount of inserted needles can therefore be explored. Current work is focused on automated planning of IC source channels, exploring plan trade-offs and generating configurations for the full treatment.

Data availability statement

The data cannot be made publicly available upon publication because they are not available in a format that is sufficiently accessible or reusable by other researchers. The data that support the findings of this study are available upon reasonable request from the authors.

Acknowledgment

Conflict of interest

Remi Nout has received research grants from the Dutch Research Council (NWO), Dutch Cancer Society (KWF), Elekta, Varian, and Accuray. The remaining authors have no relevant conflicts of interest to disclose.

Appendix. Derivation of Hessian matrix for minimum energy

The kth derivative of $B_\mu(t)$ can be written as:

$$\frac{d^k B_\mu(\tau)}{d\tau^k} = \frac{n!}{(n-k)!} \sum_{l=0}^{n-k} \Delta^k c_\mu^l b_{n-k}^l \; . \tag{A1}$$

Here, $\Delta^k c_\mu^l$ is recursively defined as the forward difference operator ($\Delta^k c_\mu^l = \Delta^{k-1} c_\mu^{l+1} - \Delta^{k-1} c_\mu^l$). The derivative can be expressed in matrix form:

$$\frac{d^k B_\mu(\tau)}{d\tau^k} = \boldsymbol{b}^k(\tau)^T D^k \boldsymbol{p}_\mu \tag{A2a}$$

where

$$\boldsymbol{b}^k(\tau)^T = \left[b_{n-k}^0, b_{n-k}^1, \ldots, b_{n-k}^{n-k} \right] \tag{A2b}$$

$$D^k = \frac{n!}{(n-k)!} \begin{bmatrix} -1 & & & 1 & \\ & \ddots & & & \ddots \\ & & -1 & & & 1 \end{bmatrix}_{[(n-k) \times n]} \tag{A2c}$$

$$\boldsymbol{p}_\mu = \left[c_{\mu j}^0, c_{\mu j}^1, \ldots, c_{\mu j}^n \right]^T \; . \tag{A2d}$$

Therefore, equation (3) can now be written as:

$$E_{\text{bend}} \approx \sum_{\mu \in \{x,y,z\}} \boldsymbol{p}_\mu{}^T D^{k^T} \overbrace{\left[\int_0^1 \boldsymbol{b}^k(\tau) \boldsymbol{b}^k(\tau)^T d\tau \right]}^{H^k} D^k \boldsymbol{p}_\mu \; . \tag{A3}$$

A component of the tensor H^k can be written as $H_{a,b}^k = \dfrac{\begin{pmatrix} n-k \\ a \end{pmatrix} \begin{pmatrix} n-k \\ b \end{pmatrix}}{\begin{pmatrix} 2n-2k \\ a+b \end{pmatrix}} \dfrac{1}{2n-2k+1}$, which follows by

multiplying two Bernstein bases and observing that the definite integral is a constant for a given n. Considering $\mathbf{x}^T = \left[\boldsymbol{p}_x^T, \boldsymbol{p}_y^T, \boldsymbol{p}_z^T \right]$, one may now write:

$$\sum_{\mu \in \{x,y,z\}} \boldsymbol{p}_\mu{}^T D^{k^T} H^k D^k \boldsymbol{p}_\mu = \mathbf{x}^T Q_0 x \; . \tag{A4}$$

Here, Q_0 contains entries of $D^{k^T} H^k D^k$ on the diagonal.

ORCID iDs

Robin Straathof ⬤ https://orcid.org/0000-0002-0396-8880
Sharline M van Vliet-Pérez ⬤ https://orcid.org/0000-0002-1189-2089
Inger-Karine K Kolkman-Deurloo ⬤ https://orcid.org/0009-0004-8452-3198
Linda S G L Wauben ⬤ https://orcid.org/0000-0002-6125-9812
Remi A Nout ⬤ https://orcid.org/0000-0001-8011-2982
Ben J M Heijmen ⬤ https://orcid.org/0000-0003-1647-0528
Linda Rossi ⬤ https://orcid.org/0000-0002-3705-2504
Jenny Dankelman ⬤ https://orcid.org/0000-0003-3951-2129
Nick J van de Berg ⬤ https://orcid.org/0000-0001-6291-990X

References

Amit G, Purdie T G, Levinshtein A, Hope A J, Lindsay P, Marshall A, Jaffray D A and Pekar V 2015 Automatic learning-based beam angle selection for thoracic IMRT *Med. Phys.* **42** 1992–2005
Attene M 2010 A lightweight approach to repairing digitized polygon meshes *Vis. Comput.* **26** 1393–406
Bailleux C, Falk A T, Chand-Fouche M E, Gautier M, Barranger E and Hannoun-Levi J M 2016 Concomitant cervical and transperineal parametrial high-dose-rate brachytherapy boost for locally advanced cervical cancer *J. Contemp. Brachytherapy* **8** 23–31
Baltas D, Kolotas C, Geramani K, Mould R F, Ioannidis G, Kekchidi M and Zamboglou N 1998 A conformal index (COIN) to evaluate implant quality and dose specification in brachytherapy *Int. J. Radiat Oncol. Biol. Phys.* **40** 515–24
Bélanger C, Aubin S, Lavallée M and Beaulieu L 2024 Simultaneous catheter and multicriteria optimization for HDR cervical cancer brachytherapy with a complex intracavity/interstitial applicator *Med. Phys.* **51** 2128–43
Bélanger C, Poulin É, Cui S, Vigneault É, Martin A G, Foster W, Després P, Cunha J A M and Beaulieu L 2020 Evaluating the impact of real-time multicriteria optimizers integrated with interactive plan navigation tools for HDR brachytherapy *Brachytherapy* **19** 607–17
Chang J-W, Choi Y-K, Kim M-S and Wang W 2011 Computation of the minimum distance between two Bézier curves/surfaces *Comput. Graph.* **35** 677–84
Chatigny P Y, Bélanger C, Poulin É and Beaulieu L 2022 Catheters and dose optimization using a modified CVT algorithm and multi-criteria optimization in prostate HDR brachytherapy *Med. Phys.* **49** 6575–87
Cobussen A, Petric P, Wulff C N, Buus S, Spejlborg H, Nielsen S K, Traberg A, Meisner B, Hokland S and Lindegaard J C 2023 Clinical outcomes using a 3D printed tandem-needle-template and the EMBRACE-II planning aims for image guided adaptive brachytherapy in locally advanced cervical cancer *Acta Oncol.* **62** 1470–8
Duan Y, Patil S, Schulman J, Goldberg K and Abbeel P 2014 Planning locally optimal, curvature-constrained trajectories in 3D using sequential convex optimization *2014 IEEE Int. Conf. on Robotics and Automation (ICRA)* (IEEE) pp 5889–95
Fauser J *et al* 2019 Planning for flexible surgical robots via Bézier spline translation *IEEE Robot. Autom. Lett.* **4** 3270–7
Fokdal L *et al* 2016 Image guided adaptive brachytherapy with combined intracavitary and interstitial technique improves the therapeutic ratio in locally advanced cervical cancer: analysis from the retroEMBRACE study *Radiother. Oncol.* **120** 434–40
Fokdal L *et al* 2018 Physician assessed and patient reported urinary morbidity after radio-chemotherapy and image guided adaptive brachytherapy for locally advanced cervical cancer *Radiother. Oncol.* **127** 423–30
Fokdal L, Tanderup K, Hokland S B, Røhl L, Pedersen E M, Nielsen S K, Paludan M and Lindegaard J C 2013 Clinical feasibility of combined intracavitary/interstitial brachytherapy in locally advanced cervical cancer employing MRI with a tandem/ring applicator in situ and virtual preplanning of the interstitial component *Radiother. Oncol.* **107** 63–68
Fortin I, Tanderup K, Haie-Meder C, Lindegaard J C, Mahantshetty U, Segedin B, Jürgenliemk-Schulz I M, Hoskin P, Kirisits C and Pötter R 2016 Image guided brachytherapy in cervical cancer: a comparison between intracavitary and combined intracavitary/interstitial brachytherapy in regard to doses to HR CTV, OARs and late morbidity—early results from the EMBRACE study in 999 patients *Brachytherapy* **15** S21
Gao F, Wu W, Lin Y and Shen S 2018 Online safe trajectory generation for quadrotors using fast marching method and Bernstein basis polynomial *2018 IEEE Int. Conf. on Robotics and Automation (ICRA)* (IEEE) pp 344–51
Garg A, Patil S, Siauw T, Cunha J A M, Hsu I C and Abbeel P 2013 An algorithm for computing customized 3D printed implants with curvature constrained channels for enhancing intracavitary brachytherapy radiation delivery *2013 IEEE Int. Conf. on Automation Science and Engineering (CASE)* (IEEE) pp 466–73
Gerlach S, Siebert F A and Schlaefer A 2024 Robust stochastic optimization of needle configurations for robotic HDR prostate brachytherapy *Med. Phys.* **51** 464–75
Gorissen B L, den Hertog D and Hoffmann A L 2013 Mixed integer programming improves comprehensibility and plan quality in inverse optimization of prostate HDR brachytherapy *Phys. Med. Biol.* **58** 1041–57
Guthier C V, Aschenbrenner K P, Müller R, Polster L, Cormack R A and Hesser J W 2016 Real-time inverse high-dose-rate brachytherapy planning with catheter optimization by compressed sensing-inspired optimization strategies *Phys. Med. Biol.* **61** 5956–72
Guthier C V, Damato A L, Hesser J W, Viswanathan A N and Cormack R A 2017 A fast inverse treatment planning strategy facilitating optimized catheter selection in image-guided high-dose-rate interstitial gynecologic brachytherapy *Med. Phys.* **44** 6117–27
Holm Å, Carlsson Tedgren Å and Larsson T 2016 Heuristics for integrated optimization of catheter positioning and dwell time distribution in prostate HDR brachytherapy *Ann. Oper. Res.* **236** 319–39
Jacobson A 2023 gptoolbox: geometry processing toolbox (available at: https://github.com/alecjacobson/gptoolbox2023)
Jo B, Park K, Shin D, Lim Y K, Jeong J H, Lee S B, Kim H-J and Kim H 2021 Feasibility study of robust optimization to reduce dose delivery uncertainty by potential applicator displacements for a cervix brachytherapy *Appl. Sci.* **11** 2592
Karabis A, Belotti P and Baltas D 2009 Optimization of catheter position and dwell time in prostate HDR brachytherapy using HIPO and linear programming *World Congress on Medical Physics and Biomedical Engineering* (Springer) pp 612–5

Kirchheiner K *et al* 2016 Health-related quality of life in locally advanced cervical cancer patients after definitive chemoradiation therapy including image guided adaptive brachytherapy: an analysis from the EMBRACE study *Int. J. Radiat Oncol. Biol. Phys.* **94** 1088–98

Kulkarni-Thaker S, Aleman D and Fenster A 2021 A row-generation approach for simultaneous multiple needle trajectory planning in radiofrequency ablation *medRxiv* (https://doi.org/10.1101/2021.06.11.21258244)

Laan R C, Nout R A, Dankelman J and van de Berg N J 2019 MRI-driven design of customised 3D printed gynaecological brachytherapy applicators with curved needle channels *3D Print. Med.* **5** 1–8

Lee C H J, Aleman D M and Sharpe M B 2014 A fast beam orientation optimization method that enforces geometric constraints in IMRT for total marrow irradiation *Int. Trans. Oper. Res.* **22** 635–45

Lee C H, Aleman D M and Sharpe M B 2011 A set cover approach to fast beam orientation optimization in intensity modulated radiation therapy for total marrow irradiation *Phys. Med. Biol.* **56** 5679–95

Lindegaard J C, Madsen M L, Traberg A, Meisner B, Nielsen S K, Tanderup K, Spejlborg H, Fokdal L U and Nørrevang O 2016 Individualised 3D printed vaginal template for MRI guided brachytherapy in locally advanced cervical cancer *Radiother. Oncol.* **118** 173–5

Logar H B Z, Hudej R and Šegedin B 2019 Development and assessment of 3D-printed individual applicators in gynecological MRI-guided brachytherapy *J. Contemp. Brachytherapy* **11** 128–36

Magné N, Chargari C, SanFilippo N, Messai T, Gerbaulet A and Haie-Meder C 2010 Technical aspects and perspectives of the vaginal mold applicator for brachytherapy of gynecologic malignancies *Brachytherapy* **9** 274–7

Mahantshetty U *et al* 2019 Vienna-II ring applicator for distal parametrial/pelvic wall disease in cervical cancer brachytherapy: an experience from two institutions: clinical feasibility and outcome *Radiother. Oncol.* **141** 123–9

Mehdi S B, Choe R, Cichella V and Hovakimyan N 2015 Collision avoidance through path replanning using Bézier curves *AIAA Guidance, Navigation, and Control Conf.* (AIAA) pp 1–23

Mellinger D and Kumar V 2011 Minimum snap trajectory generation and control for quadrotors *2011 IEEE Int. Conf. on Robotics and Automation* (IEEE) pp 2520–5

Moerman K M 2018 GIBBON: the geometry and image-based bioengineering add-On *J. Open Source Softw.* **3** 1–4

Morén B, Larsson T and Tedgren Å C 2021 Optimization in treatment planning of high dose-rate brachytherapy—review and analysis of mathematical models *Med. Phys.* **48** 2057–82

Nilsson S, Moutrie Z, Cheuk R, Chan P, Lancaster C, Markwell T, Dawes J and Back P 2015 A unique approach to high-dose-rate vaginal mold brachytherapy of gynecologic malignancies *Brachytherapy* **14** 267–72

Oud M, Kolkman-Deurloo I-K, Mens J-W, Lathouwers D, Perkó Z, Heijmen B and Breedveld S 2020 Fast and fully-automated multi-criterial treatment planning for adaptive HDR brachytherapy for locally advanced cervical cancer *Radiother. Oncol.* **148** 143–50

Patil S, Pan J, Abbeel P and Goldberg K 2015 Planning curvature and torsion constrained ribbons in 3D with application to intracavitary brachytherapy *IEEE Trans. Autom. Sci. Eng.* **12** 1332–45

Petric P, Hudej R, Al-Hammadi N and Šegedin B 2016 Virtual modelling of novel applicator prototypes for cervical cancer brachytherapy *Radiol. Oncol.* **50** 433–41

Pötter R *et al* 2007 Clinical impact of MRI assisted dose volume adaptation and dose escalation in brachytherapy of locally advanced cervix cancer *Radiother. Oncol.* **83** 148–55

Pötter R *et al* 2018 The EMBRACE II study: the outcome and prospect of two decades of evolution within the GEC-ESTRO GYN working group and the EMBRACE studies *Clin. Transl. Radiat. Oncol.* **9** 48–60

Poulin E, Fekete C A, Létourneau M, Fenster A, Pouliot J and Beaulieu L 2013 Adaptation of the CVT algorithm for catheter optimization in high dose rate brachytherapy *Med. Phys.* **40** 1–9

Rajesh G and Khatait J P 2021 Deformation modeling of a flexible instrument using a Bézier curve *J. Med. Devices* **15** 1–7

Reijtenbagh D, Godart J, de Leeuw A, Seppenwoolde Y, Jürgenliemk-Schulz I, Mens J-W, Nout R and Hoogeman M 2022 Multi-center analysis of machine-learning predicted dose parameters in brachytherapy for cervical cancer *Radiother. Oncol.* **170** 169–75

Richter C, Bry A and Roy N 2016 Polynomial trajectory planning for aggressive quadrotor flight in dense indoor environments *Robotics Research: The 16th Int. Symp. ISRR* (Springer) pp 649–66

Rossi L *et al* 2024 Clinician Preferred, Fast Autoplanning in Cervical Cancer Brachytherapy Using BiCycle *Radiat. Oncol. J.* **194** S215–7

Sadowski K L *et al* 2017 Exploring trade-offs between target coverage, healthy tissue sparing, and the placement of catheters in HDR brachytherapy for prostate cancer using a novel multi-objective model-based mixed-integer evolutionary algorithm *Proc. Genetic and Evolutionary Computation Conf.* (ACM) pp 1224–31

Serban M *et al* 2020 Ring versus ovoids and intracavitary versus intracavitary-interstitial applicators in cervical cancer brachytherapy: results from the EMBRACE I study *Int. J. Radiat Oncol. Biol. Phys.* **106** 1052–62

Serban M, Fokdal L, Nielsen S K, Hokland S B, Hansen A T, Spejlborg H, Rylander S, Petric P, Lindegaard J C and Tanderup K 2021 Characterization of combined intracavitary/interstitial brachytherapy including oblique needles in locally advanced cervix cancer *Brachytherapy* **20** 796–806

Siauw T, Cunha A, Berenson D, Atamtürk A, Hsu I-C, Goldberg K and Pouliot J 2012 NPIP: a skew line needle configuration optimization system for HDR brachytherapy *Med. Phys.* **39** 4339–46

Straathof R *et al* 2024 Multibody dynamic modeling of the behavior of flexible instruments used in cervical cancer brachytherapy *Med. Phys.* **51** 3698–710

Sunderland K, Woo B, Pinter C and Fichtinger G 2015 Reconstruction of surfaces from planar contours through contour interpolation *Proc. SPIE* **9415** 94151R1-8

Tanderup K, Hellebust T P, Lang S, Granfeldt J, Pötter R, Lindegaard J C and Kirisits C 2008 Consequences of random and systematic reconstruction uncertainties in 3D image based brachytherapy in cervical cancer *Radiother. Oncol.* **89** 156–63

van der Meer M C, Pieters B R, Niatsetski Y, Alderliesten T, Bel A and Bosman P A N 2018 Better and faster catheter position optimization in HDR brachytherapy for prostate cancer using multi-objective real-valued GOMEA *Proc. Genetic and Evolutionary Computation Conf.* pp 1387–94

Veltkamp R C and Wesselink W 1995 Modeling 3D curves of minimal energy *Comput. Graph. Forum* **14** 97–110

Wang C, Gonzalez Y, Shen C, Hrycushko B and Jia X 2021 Simultaneous needle catheter selection and dwell time optimization for preplanning of high-dose-rate brachytherapy of prostate cancer *Phys. Med. Biol.* **66** 1–13

Wiebe E, Easton H, Thomas G, Barbera L, D'Alimonte L and Ravi A 2015 Customized vaginal vault brachytherapy with computed tomography imaging-derived applicator prototyping *Brachytherapy* **14** 380–4

Yusufaly T I *et al* 2020 A knowledge-based organ dose prediction tool for brachytherapy treatment planning of patients with cervical cancer *Brachytherapy* **19** 624–34

Zhang D, Yang Z, Jiang S, Zhou L, Zhou Z and Wang W 2019 Individualized and inverse optimized needle configuration for combined intracavitary-interstitial brachytherapy in locally advanced cervical cancer *J. Cancer Res. Ther.* **15** 1589–96

Zhao Y, Wang Y, Zhou M and Wu J 2019 Energy-optimal collision-free motion planning for multiaxis motion systems: an alternating quadratic programming approach *IEEE Trans. Autom. Sci. Eng.* **16** 327–38